

Versatile Sequential Casting Processing for Highly Efficient and Stable Binary Organic Photovoltaics

Chengliang He, Youwen Pan, Guanghao Lu, Baohua Wu, Xinxin Xia, Chang-Qi Ma, Zeng Chen, Haiming Zhu, Xinhui Lu, Wei Ma, Lijian Zuo,* and Hongzheng Chen*

Forming an ideal bulk heterojunction (BHJ) morphology is a critical issue governing the photon to electron process in organic solar cells (OSCs). Complementary to the widely-used blend casting (BC) method for BHJ construction, sequential casting (SC) can also enable similar or even better morphology and device performance for OSCs. Here, BC and SC methods on three representative donor:acceptor (D:A) blends are utilized, that is, PM6:PC₇₁BM, PM6:IT-4F and PM6:L8-BO. Higher power conversion efficiencies (PCEs) in all cases by taking advantage of beneficial morphology from SC processing are achieved, and a champion PCE of 18.86% (certified as 18.44%) based on the PM6:L8-BO blend is reached, representing the record value among binary OSCs. The observations on phase separation and vertical distribution inspire the proposal of the swelling–intercalation phase-separation model to interpret the morphology evolution during SC processing. Further, the vertical phase segregation is found to deliver an improvement of device performance via affecting the charge transport and collection processes, as evidenced by the D:A-ratio-dependent photovoltaic properties. Besides, OSCs based on SC processing show advantages on device photostability and upscale fabrication. This work demonstrates the versatility and efficacy of the SC method for BHJ-based OSCs.

of OSCs consists of a layered structure with an active layer sandwiched between cathode and anode, as buffered by the interfacial charge-transporting layers. The active layer is the most important ingredient to function as the light-absorbing, charge generating and transporting layer. The most popular and efficient active layer structure consists of a donor:acceptor (D:A) blend film with a very tricky nanoscale phase-separated interpenetrating network, or the so-called “bulk heterojunction (BHJ) structure”,^[7] in order to conquer the high exciton binding energy and bipolar charge-transporting limitations and enable fast exciton dissociation and smooth charge transport, respectively.^[8] The rapid progress in molecule design, morphology control, device engineering, etc., has greatly boosted the device performance of OSCs to make them more competitive with their inorganic counterparts.^[9–25] Currently, record power conversion efficiencies (PCEs) of

1. Introduction

Organic solar cells (OSCs) have aroused the enthusiasm of researchers and achieved rapid development in the past few decades, due to their advantages of superior flexibility, good selective absorption for transparency, lightweight, low-cost production via solution processing, etc.^[1–6] The device structure

19.6% and 20.2% have been achieved for single-junction ternary device and tandem device, respectively.^[26,27]

Among all of the factors governing the photon to electron process in OSCs, forming an ideal BHJ morphology is the trickiest one, which requires not only a proper D:A pair with critical miscibility, but also delicate control on the phase-separation kinetics.^[8] Constructing BHJ includes two main

C. He, Y. Pan, L. Zuo, H. Chen
State Key Laboratory of Silicon Materials
MOE Key Laboratory of Macromolecular Synthesis and Functionalization
International Research Center for X Polymers
Department of Polymer Science and Engineering
Zhejiang University
Hangzhou 310027, P. R. China
E-mail: zjuzlj@zju.edu.cn; hzchen@zju.edu.cn
G. Lu
Frontier Institute of Science and Technology
Xi'an Jiaotong University
Xi'an 710054, P. R. China

B. Wu, W. Ma
State Key Laboratory for Mechanical Behavior of Materials
Xi'an Jiaotong University
Xi'an 710049, P. R. China
X. Xia, X. Lu
Department of Physics
Chinese University of Hong Kong
New Territories
Hong Kong 999077, P. R. China
C.-Q. Ma
i-Lab & Printable Electronics Research Centre
Suzhou Institute of Nano-tech and Nano-bionics
Chinese Academy of Sciences
Suzhou 215123, P. R. China
Z. Chen, H. Zhu
Department of Chemistry
Zhejiang University
Hangzhou 310027, P. R. China

 The ORCID identification number(s) for the author(s) of this article can be found under <https://doi.org/10.1002/adma.202203379>.

DOI: 10.1002/adma.202203379

methods: bottom-to-top bulk phase separation and top-to-bottom permeation. Usually, the active layer is processed by blend casting (BC), where the donor and acceptor are well premixed in solution.^[28] The thin solid film is formed by evaporating solvent from the wet film, as accompanied with phase-separation, which is mediated by the choice of solvent and processing conditions. Complementary to the above-mentioned BC method, the sequential casting (SC), also known as layer-by-layer processing, in which the donor and acceptor are deposited sequentially, provides an avenue for morphology control aiming at ordered molecular packing through top-to-bottom permeation.^[29–32] The first layer undergoes solvent evaporation to form a crystalline film, which could be adjusted by the solvent choice and drying time. The second layer permeates into the first layer to form a phase-separated structure, which is dictated by the crystallinity and miscibility between the donor and acceptor. It is interesting to observe that the devices processed with SC exhibit similar or even better device performance.^[17,33–37] Sun et al. combined the fibril network layer and the two-step sequential deposition method to control morphology, which is insensitive to the polymer batches with a higher PCE than that of BC.^[33] Jen et al. reported that a pseudo-bilayer architecture processed by SC possesses longer exciton diffusion length which benefited from higher film crystallinity, thus achieving a higher PCE.^[34] Our group combined the SC procedure and the ternary strategy to fabricate the device and achieved the highest efficiency at the time.^[17] Besides, researchers found that SC shows advantages in the blade-coating procedure and upscale fabrication.^[35,36] Nevertheless, the mechanism underlying how the SC processing enables the ideal BHJ morphology is still unclear, as well as how the featured morphology processed with SC will affect the optoelectronic properties of OSCs. This further hinders the discovery of more delicate control on the processing to fully explore the potential of SC for high performance.

To address this issue, here we have studied the effect of SC processing on three representative D:A blends, that is, PM6:PC₇₁BM, PM6:IT-4F and PM6:L8-BO, which cover the record material systems within the past dozen years,^[38–40] and compared them with the conventional BC processing. Through the multidimensional morphology observations from resonant soft X-ray scattering (RSoXS), grazing-incidence wide-angle X-ray scattering (GIWAXS), atomic force microscopy (AFM), film-depth-dependent light absorption spectroscopy (FLAS) and depth-profiling X-ray photoelectron spectroscopy (D-XPS), etc., it is interesting to find that the SC processing yields a BHJ structure with similar phase domains, film crystallinity and vertical phase-segregation, but a more delicate nanoscale phase-separated interpenetrating network when compared to BC processing, while countering to the intuitive understanding of acceptor permeating from top to bottom, for example, the vertical phase segregation of acceptor actually can be richer at the bottom with SC processing.^[41,42] These observations inspire us to propose the swelling–intercalation phase-separation (SIPS) model to interpret the morphology evolution during the SC processing. Further, we studied the effect of vertical phase separation on the charge collection of OSCs, and find the composition-dependent electron and hole carrier mobility determines the efficacy of vertical phase separation for charge transport and

collection. By taking advantage of beneficial morphology from SC processing, a champion PCE of 18.86% (certified as 18.44%) for the PM6:L8-BO blend is reached, as is higher than that of the BC processed one. Notably, this result also represents the record value among binary OSCs, and demonstrates the potential of SC method for high-performance OSCs. We then applied the SC processing in upscaled device, and reached a high efficiency of 16.50%. In addition to the PCE increment, the device photostability is also improved with SC processing.

2. Results and Discussion

2.1. Device Performance

First, we studied the efficacy of SC processing on device performance of OSCs. Three representative material systems, that is, PM6 as donor to blend with acceptor of PC₇₁BM, IT-4F and L8-BO, respectively, are selected by considering their record performance in the past dozen years.^[38–40] The chemical structures of these materials are depicted in **Figure 1a**. All of them have been demonstrated to form good BHJ structure with BC processing. The energy levels determined by cyclic voltammetry and absorption profiles of these materials are shown in **Figure 1b,c** and **Figure S1**, Supporting Information. Herein, the devices with a conventional structure of ITO/PEDOT:PSS/active layer/PFN-Br/Ag were adopted to examine the effect of different processing on device performance (**Figure 1d**). The BC-type devices were fabricated via spin-coating from a mixed D:A solution, while the SC-type devices were fabricated via spin-coating from PM6 solution and acceptor solution in sequence. Detailed device fabrication conditions and characterizations are summarized in **Tables S1–S4**, Supporting Information. **Figure 1e** shows the current density–voltage (*J*–*V*) curves of the PM6:PC₇₁BM, PM6:IT-4F, and PM6:L8-BO blends in BC-type device and SC-type device. Detailed photovoltaic parameters are summarized in **Table 1**. For the best-performing PM6:L8-BO system, the BC-type device exhibits an open-circuit voltage (*V*_{oc}) of 0.885 V, a short-circuit current density (*J*_{sc}) of 26.25 mA cm^{−2} and a fill factor (FF) of 78.47%, leading to a PCE of 18.18%. When utilizing the SC processing way, the *J*_{sc} (26.61 mA cm^{−2}) and the FF (80.39%) were improved with *V*_{oc} (0.883 V) almost unchanged (we investigated the luminescence abilities through electroluminescence quantum efficiency of the devices processed by BC and SC methods [**Figure S2**, Supporting Information], and the values are very close), yielding a PCE of 18.86%. Notably, the PCE of 18.86% is the highest among binary OSCs up to data (**Figure 1f**). Besides, the PCE improvement obtained by SC processing is also found in the PM6:PC₇₁BM and PM6:IT-4F systems (**Figure 1e** and **Table 1**). It is interesting to observe that the SC processing can generally enable better device performance for OSCs. And a general trend can be derived that both of FF and *J*_{sc} get enhanced, while the *V*_{oc} slightly decreases with SC processing, compared to those of BC processing. As a result, it is argued that the SC might be a more superior processing method for high-performance OSCs. Further, the best-performing device is sent to a third authority for certification, and a certified efficiency of 18.44% from the National Institute of Metrology (NIM), China was obtained for

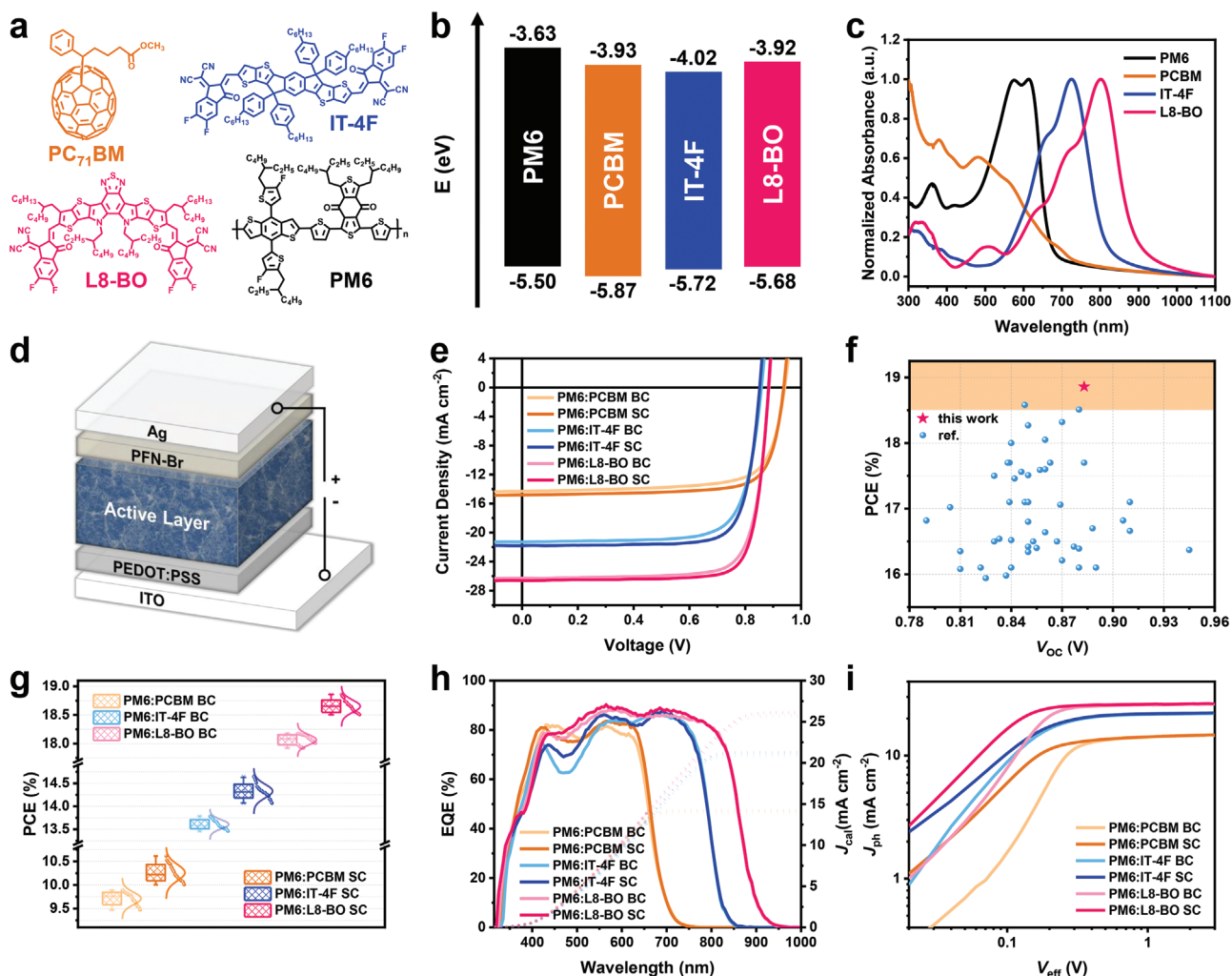


Figure 1. a) Chemical structures of PC₇₁BM, IT-4F, L8-BO and the polymer donor PM6. b) Energy level diagram determined by cyclic voltammetry. c) UV-vis absorption spectra of the materials in films. d) A schematic illustration of the conventional device structure. e) J-V curves of the optimal devices. f) Comparison of binary devices between this work and references (original data are summarized in Table S14, Supporting Information). g) PCE statistics of 30 cells for each D:A system. h) EQE curves of the optimal devices. i) J_{ph}-V_{eff} curves of the optimal devices.

the SC-type encapsulated device (Table 1 and certification report in Supporting Information). It is worthy to note that this result is the highest among the certified binary OSCs. This further confirms the superiority of SC processing for OSCs.

To confirm the PV performance variations with different processing, we fabricated more devices to extract and compare the average values and standard deviations of device parameters. Figure 1g and Table 1 provide the PCE statistics from 30 devices for each system. The statistical PCE distributions of all the three systems indicate that the SC-type devices show better performance than the BC-type devices and the variation trend of averaged device parameter is the same as the champion ones, confirming that the SC method exhibits advantages over the BC method for high device performance.

To figure out the origin of improved J_{sc} with SC processing, the external quantum efficiency (EQE) test was performed (Figure 1h and Table 1). The integrated values (J_{cal}) from the EQE curves are very close to those from the J-V curves, validating the device performance derived from J-V measurement.

While it is interesting to observe that the shape of EQE actually gets changed from BC to SC processing for the PM6:PC₇₁BM and PM6:IT-4F systems, but remains for the PM6:L8-BO system. These results suggest that both optical interference and internal carrier dynamics play a role for the improvement in J_{sc}.^[34] Further, to understand the mechanism underlying the improved FF with SC processing, we studied the carrier dynamics in OSCs by investigating the relationship between photocurrent density and effective voltage of the devices to characterize the bias-dependent charge separation and collection behavior (Figure 1i and Table S5, Supporting Information).^[43] The calculated exciton dissociation efficiencies (P_{diss}) in BC-type devices are 97.02%, 98.09% and 98.36% for the PM6:PC₇₁BM, PM6:IT-4F and PM6:L8-BO systems, respectively, while being 97.84%, 98.29% and 98.90% for SC-type devices. The calculated charge collection efficiencies (P_{coll}s) are 83.06%, 83.18% and 89.09% for the PM6:PC₇₁BM, PM6:IT-4F and PM6:L8-BO systems, respectively, while being 85.12%, 85.03% and 90.56% in SC-type devices. It is found that SC-type devices

Table 1. Photovoltaic parameters of the optimal devices.

Active layer	V_{oc} [V]	J_{sc} [mA cm^{-2}]	J_{cal} [mA cm^{-2}] ^{a)}	FF [%]	PCE [%] ^{b)}
PM6:PC ₇₁ BM (BC)	0.942 (0.942 ± 0.005)	14.32 (14.15 ± 0.14)	13.90	73.33 (72.82 ± 0.54)	9.89 (9.71 ± 0.13)
PM6:PC ₇₁ BM (SC)	0.938 (0.941 ± 0.006)	14.81 (14.48 ± 0.19)	14.20	76.58 (75.46 ± 0.80)	10.61 (10.26 ± 0.17)
PM6:IT-4F (BC)	0.858 (0.861 ± 0.002)	21.28 (21.00 ± 0.18)	20.87	75.47 (75.34 ± 0.42)	13.78 (13.61 ± 0.10)
PM6:IT-4F (SC)	0.853 (0.852 ± 0.002)	21.75 (21.44 ± 0.27)	21.24	78.85 (78.44 ± 0.60)	14.65 (14.33 ± 0.15)
PM6:L8-BO (BC)	0.885 (0.884 ± 0.002)	26.25 (26.20 ± 0.14)	25.72	78.47 (78.24 ± 0.33)	18.18 (18.06 ± 0.09)
PM6:L8-BO (SC)	0.883 (0.881 ± 0.003)	26.61 (26.61 ± 0.14)	26.10	80.39 (79.74 ± 0.33)	18.86 (18.65 ± 0.10)
PM6:L8-BO (SC)	0.881	26.52		79.0	18.44 ^{c)}

^{a)} Integrated current density from EQE curve; ^{b)} Average PCE from 30 devices; ^{c)} Certified by NIM, China.

show a subtle advantage in P_{diss} and a more obvious advantage in P_{coll} compared with BC-type devices, affording the improved FF. As a result, it is argued that the SC processing method is practical and universal for PCE improvement with gain in J_{sc} and FF via changing both the light trapping properties and the carrier dynamics.

2.2. Film Morphology

Considering that the different processing mostly affects the morphology of the active layer, we put emphasis on resolving the film morphology characteristics of these systems with different processing. First, we conducted RSoXS tests to analyze the phase separation (Figure 2a and Figure S3 and Table S6, Supporting Information), which can give information on the phase separation size and phase purity.^[44,45] These parameters are essentially important for charge generation and charge transport, as unveiled in previous work.^[44] For the PM6:PC₇₁BM system, the difference in phase purity between the BC-type and SC-type films is negligible, and the average phase domain size of the SC-type film is 13.36 nm, which is smaller than that from BC processing (14.70 nm). For nonfullerene systems (PM6:IT-4F and PM6:L8-BO), it is interesting to observe that the phase purity of SC-type film is lower than that of BC-type. The average domain sizes decrease from 20.98 to 19.10 nm for the PM6:L8-BO system, but increased from 17.96 to 21.93 nm for the IT-4F system with SC processing. The phase domain size of all the above systems seems to be within the range of exciton diffusion for efficient exciton separation or charge generation. Intuitively, during the SC processing, the acceptor will permeate into PM6 from top to bottom, and thus is expected to form a purer grain due to the pre-formed pristine PM6 film. As a result, it is counterintuitive to observe the reduced phase purity during the SC processing, according to the infiltration process. Instead, the phase purity seems to be more closely related to other parameters than the “permeation” process.

GIWAXS characterization was performed to investigate the molecular packing and the crystalline properties.^[46] As shown

in Figure 2b,c, and Figure S4 and Table S7, Supporting Information, there is no significant difference between BC-type and SC-type films in the in-plane direction. In the out-of-plane direction, for the PM6:PC₇₁BM system, its diffraction peaks in SC-type film are not as sharp as observed in BC-type film ($q_z = 1.31 \text{ \AA}^{-1}$ [$d = 4.79 \text{ \AA}$] and $q_z = 1.68 \text{ \AA}^{-1}$ [$d = 3.74 \text{ \AA}$]). For the PM6:IT-4F system, the π - π stacking becomes denser in SC-type film, with the diffraction peaks located at $q_z = 1.74 \text{ \AA}^{-1}$ ($d = 3.61 \text{ \AA}$) in BC-type film and $q_z = 1.77 \text{ \AA}^{-1}$ ($d = 3.55 \text{ \AA}$) in SC-type films. Besides, SC-type film presents slightly larger crystal correlation length (CCL) (35.8 \AA) than BC-type film (34.1 \AA). For the PM6:L8-BO system, no obvious change in the stacking distance ($d = 3.63 \text{ \AA}$) and a small increase in the crystal correlation length (CCL) (28.3 \AA versus 26.3 \AA) were obtained from BC-type film to SC-type film. In general, for fullerene and nonfullerene systems, the overall difference between the films obtained by the two processing methods in GIWAXS is not very obvious, suggesting the film phase-separation might be similar with SC and BC processing ways. The difference may exist in the interaction of solvent/acceptor with donor during SC process.

Atomic force microscopy (AFM) measurement was conducted to study the surface morphology. Combining the height and phase images shown in Figure 2d and Figures S6 and S7, Supporting Information, we found that nanofiber-like morphology could be observed in all the three blends, indicating the well-formed interpenetrating networks. A similar fibrillar network structure was also reported in a polymer donor D18 based active layer.^[47,48] Particularly, it is found that a more delicate nanoscale phase-separated interpenetrating network is formed through SC method (Figure S8, Supporting Information). These results can be attributed to the intercalation of acceptor to the donor after solvent swelling during SC process. In addition, we tested the pristine D/A film as shown in Figure S7, Supporting Information. It is found the surface of the acceptor is relatively rough, and the texture of the donor could be enhanced after being swelled by chloroform due to that the amorphous regions of lower density in a semicrystalline polymer film are more susceptible to swelling than the crystalline regions,^[17,29] which

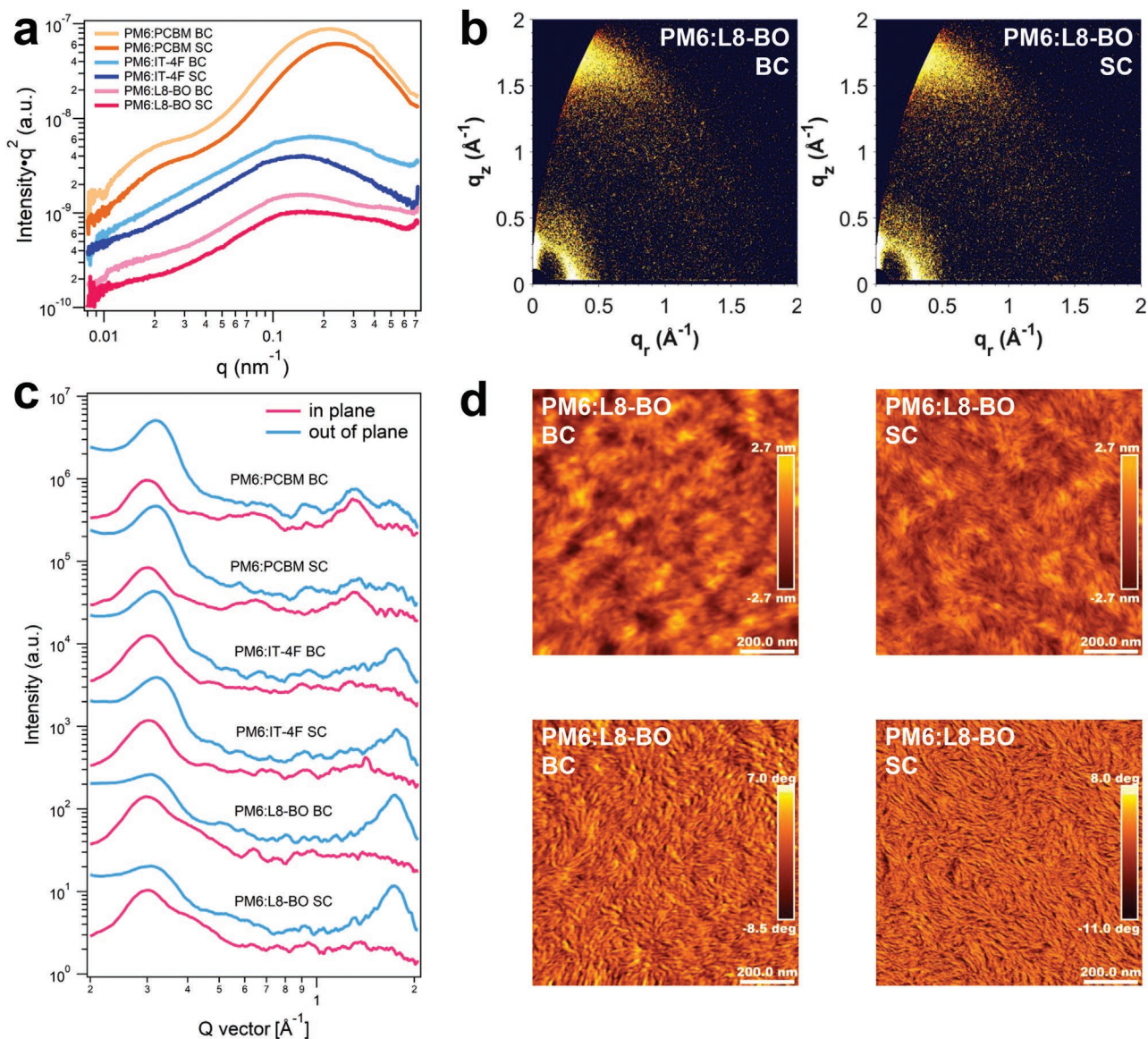


Figure 2. a) RSoXS profiles of the blend films based on different process conditions. b) 2D GIWAXS images of PM6:L8-BO blend films from the BC and SC methods. c) GIWAXS intensity profiles of the three blend films along the in-plane (blue lines) and out-of-plane (red lines) directions. d) AFM height (top) and phase (bottom) images of PM6:L8-BO blend films from BC and SC methods.

could lay the foundation for the formation of a delicate interpenetrating network in the SC blend films.

To further investigate the difference in the vertical phase segregation, which has been demonstrated as the major difference for films processed from BC and SC, we performed the FLAS and the detailed calculations could be found in Figure 3 and Figure S9–S12, Supporting Information).^[49–51] FLAS of BC-type and SC-type films of the PM6:L8-BO blend are displayed in Figures 3a and 3b. Figure 3c,d provide the components distribution profiles at different film-depths to give a re-aligned sight of D:A content for clarity and we combined them in the same figure for clearer comparison in Figure S12a, Supporting Information. It can be found that PM6 and L8-BO show obvious inhomogeneous distribution along the vertical direction for both BC and SC processed films. For both cases, the PM6 enriches at

both the top and bottom interface. However, it is observed that the SC processed film has less PM6 enrichment at both interfaces. In addition, it is also found that PM6 enriches at both top and bottom interfaces in the two processing cases for the PM6:IT-4F system (Figure S10, Supporting Information). For the PM6:PC₇₁BM system (Figure S9, Supporting Information), in the BC-type films the acceptor enriches at both top and bottom interfaces, while in the SC-type film, PM6 at both ends tends to converge toward the middle. Interestingly, vertical distributions in all the three systems are a contrast to conventional cognition that the formation of vertical phase-separated structures with D/A enrichment at both electrodes in sequential deposition process for both fullerene- and nonfullerene-based systems.^[41,42] We then performed the D-XPS to investigate the relative D:A ratio along with depth throughout the whole film. Taking the

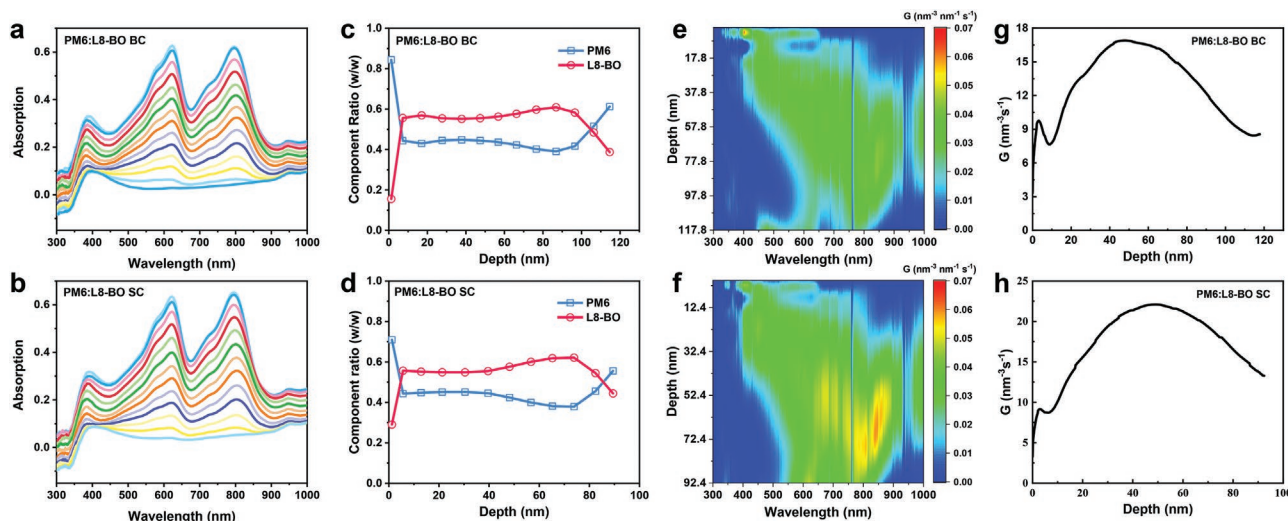


Figure 3. a,b) Film-depth-dependent light absorption spectra of BC-type and SC-type films in PM6:L8-BO system. c,d) Components distribution profiles at different film-depths. e,f) Calculated exciton generation contours in BC-type films (e) and SC-type films (f). g,h) Film-depth-dependent exciton generation rates as obtained by integration of (e) and (f) along the wavelength direction.

best-performing PM6:L8-BO system for example, since both PM6 and L8-BO contain fluorine (F), while only L8-BO contains nitrogen (N), we attribute the F element to both PM6 and L8-BO, N element to only L8-BO. Based on the F/N atom ratio, the polymer weight content at different depths can be calculated as shown in Figures S13 and S14 and Tables S8 and S9, Supporting Information. Detailed calculation method could be found in the note of Figure S13, Supporting Information. For PM6:L8-BO films from BC and SC processing, the PM6 enriches at both top and bottom interfaces. It can be inferred that the D-XPS results are consistent with the FLAS results (Figure 3) to a certain extent.

Figure 3e,f show the distribution of charge generation intensity (exciton generation rate) within the photovoltaic devices, which is numerically simulated from the FLAS in combination with a modified transfer-matrix optical model.^[50] The excitons

are mainly generated at the center and the bottom of the blend films. Particularly, the density of exciton in the SC-type film is much higher than that of the BC-type film in the region from 600 to 900 nm, which contributes to the improved EQE and J_{SC} . According to Figure 3f, L8-BO with an absorption peak ≈ 800 nm contributes more to the exciton generation relative to PM6 with an absorption edge ≈ 600 nm, which agrees well with the composition distribution extracted from the FLAS.

The counterintuitive phenomena observed above, for example, the phase purity and vertical phase segregation, suggest a different process dominating the phase-separation kinetics rather than the inter-filtration of acceptor from top to bottom. Considering that the formed morphology with SC processing is actually a perfect BHJ structure compared to BC (Figure 4a), a phase-separation process resemblance

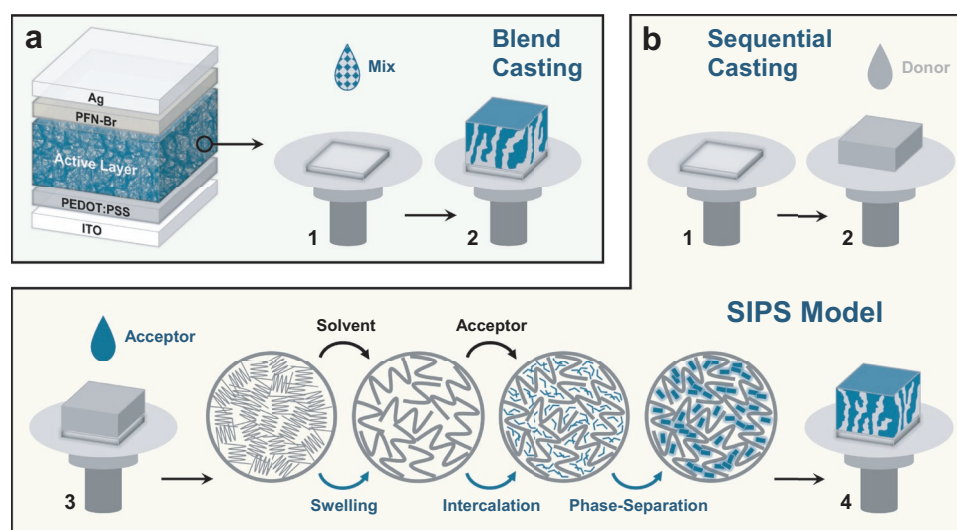


Figure 4. a) Diagram of fabrication procedures for BC-type devices. b) Diagram of fabrication procedures for SC-type devices and the proposed swelling–intercalation phase-separation (SIPS) model.

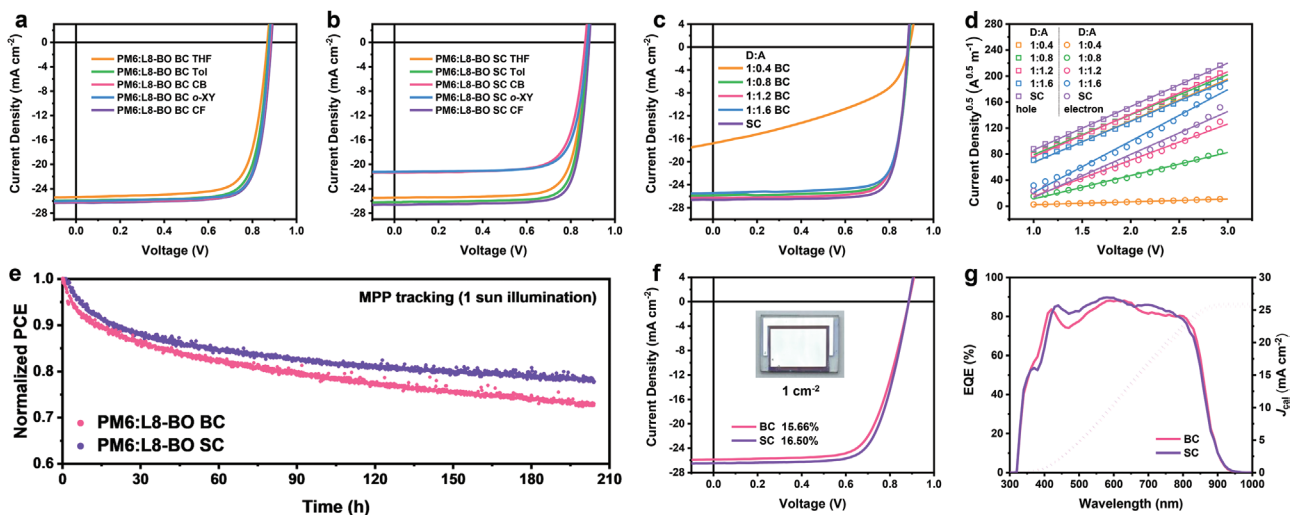


Figure 5. a) J - V curves of the optimal devices based on PM6:L8-BO system processed via BC method with different solvents. b) J - V curves of the optimal devices based on PM6:L8-BO system processed via the SC method with different solvents. c) J - V curves of the optimal devices based on the PM6:L8-BO system processed via the BC and SC methods. d) Charge-carrier mobility of the optimal devices based on the PM6:L8-BO system processed via the BC and SC methods. e) Photostability comparison between BC-type and SC-type devices based on the PM6:L8-BO system. f) J - V curves of the optimal 1 cm² devices based on the PM6:L8-BO system. g) EQE curves of the optimal 1 cm² devices based on the PM6:L8-BO system.

to BC should occur during the SC processing. Here, we propose the SIPS model to interpret the whole process, as shown in Figure 4b. With depositing the acceptor solution onto the PM6 film, the solvent, that is, chloroform, will first swell PM6 polymer to form a gel-like structure. Following this, the acceptor molecules will intercalate into the swollen polymer matrix to form a well-mixed wet blend film. Finally, during the solvent evaporation, the phase-separation will occur in the well-mixed donor-acceptor blend film. As a result, the SC will undergo similar phase-separation and yield similar morphology to the BC processing. This model well explains the formation of very good BHJ and the general observation on the efficacy of SC for high-performance OSCs. Moreover, this model explains the counterintuitive observation on phase purity and vertical phase segregation, which are determined by the miscibility between the donor and acceptor,^[17] and the solvent permeation and evaporation kinetics.^[28] According to the SIPS model, the solvent will first “swell” the pristine polymer, and this composes an exact solvent selection criterion for solvent: the solubility and boiling point must be in a proper range. This has been confirmed by using different processing solvents with different boiling point (BP) and solubility for BC and SC processing (Figure 5a,b, and Figures S15 and S16 and Tables S2 and S4, S10 and S12, Supporting Information). For example, by selecting the tetrahydrofuran (THF), which shows comparable BP but low solubility compared to chloroform (CF), an obvious drop in PCE is observed, as attributed to the poor swelling process (Figure 5b and Table S11, Supporting Information). By using chlorobenzene (CB) showing similar solubility but higher BP compared to CF, the long dwelling time of CB could overreact with the PM6 layer to form a dense solution layer rather than a swelling polymer matrix, and thus cause poor morphology and low device performance (Figure 5b and Table S11, Supporting Information). Compromising the BP and solubility, the toluene (Tol) recovers most of the efficiency compared to

THF and CB. Further, a poor efficiency is expected when using an even higher BP solvent, that is, *o*-xylene (*o*-XY) (Figure 5b and Table S11, Supporting Information). These observations support the SIPS model well, and confirm the above solvent selection rule derived from SIPS model (more detailed analysis can be found in the Solvent Selection Rules Section, Supporting Information).

2.3. Composition-Dependent Carrier Dynamics

We observe that the improved device performance is partially attributed to the increased FF (statistics in Table 1 and Figure S17a, Supporting Information), which is closely related to the carrier dynamics and subsequently the morphology. Considering the difference of lateral phase-separated morphology for films processed from SC and BC is actually within the optimal ranges, we focus on the effect of vertical phase segregation on the carrier dynamics, and pay particular attention on the ratio-dependent photovoltaic properties. Hence, we chose the best-performing PM6:L8-BO blend as the object and selected the D:A ratios of four representative positions (1:0.4, 1:0.8, 1:1.2, and 1:1.6 by wt.) according to its vertical distribution characteristics (Figure S12b, Supporting Information) to fabricate the device for charge dynamic study. Figure 5c shows the J - V curves of the BC-type devices based on different D:A ratios and the SC-type device. Detailed photovoltaic parameters are summarized in Table 2. The BC-type devices deliver PCEs of 6.51%, 18.04%, 18.18% and 17.70% for the ratio of 1:0.4, 1:0.8, 1:1.2 and 1:1.6, respectively. Figure S17b, Supporting Information, provides the EQE curves of the corresponding devices. It can be inferred that the ratio of 1:1.2 is the best for device operation and this ratio occupies the largest proportion in the vertical distribution.

As shown in Figure S17c, Supporting Information, the SC-type device possesses the highest P_{diss} and P_{coll} values (98.90%

Table 2. Photovoltaic parameters of the optimal devices based on different device types and different D:A ratios.

Active layer	V_{oc} [V]	J_{sc} [mA cm ⁻²]	FF [%]	PCE [%]	μ_e^a [$\times 10^{-4}$ cm ² V ⁻¹ s ⁻¹]	μ_h^b [$\times 10^{-4}$ cm ² V ⁻¹ s ⁻¹]
PM6:L8-BO BC (1:0.4)	0.890	16.78	43.76	6.51	0.0622	13.8
PM6:L8-BO BC (1:0.8)	0.888	25.84	78.82	18.04	4.24	12.7
PM6:L8-BO BC (1:1.2)	0.885	26.25	78.47	18.18	10.3	14.3
PM6:L8-BO BC (1:1.6)	0.885	25.42	78.70	17.70	21.0	13.3
PM6:L8-BO SC	0.883	26.61	80.39	18.86	14.6	15.0

^a)Electron mobility from SCLC method; ^b)Hole mobility from SCLC method.

and 90.56%), while the BC-type device under 1:0.4 ratio exhibits the worst P_{diss} and P_{coll} values (72.92% and 43.24%). Charge separation and collection behaviors are less affected with the D:A ratios ranging from 1:0.8 to 1:1.6. To investigate the charge transport after charge separation, the space-charge-limited current method was utilized to examine the charge-carrier mobility in the blends (Figure 5d and Table 2). In BC-type devices, with the increase of the acceptor ratio, the electron mobility increases gradually, while the hole mobility remains basically unchanged. Among them, the value of μ_e/μ_h for the device based on the 1:1.2 ratio is the closest to 1, indicating that the charge transport is the most balanced. This suggests that vertical phase-segregation affects the carrier dynamics by influencing the electron collection properties. Compared with the BC-type device under 1:1.2 ratio, the SC-type device exhibits a slightly higher mobility, and its value of μ_e/μ_h is 1.03. It can be seen from Figure 3h that the SC-type film has the highest exciton density in the middle, with the extremely balanced mobility, it is favorable to improve the device performance.

Further, the charge recombination behavior was then investigated by light intensity (P_{light})-dependent J_{sc} and V_{oc} .^[52] As shown in Figure S17d, Supporting Information, from the n values derived from the P_{light} -dependent V_{oc} , it is suggested that monomolecular recombination is the dominant recombination type and the BC-type device under 1:0.4 ratio suffers monomolecular recombination severely. The α values of current density versus P_{light} indicate that the SC-type device can suppress the trap-mediated monomolecular charge recombination and facilitate the charge extraction, and this contributes to the high J_{sc} and FF. The suppressed recombination is also consistent with the balanced charge transport mentioned above.

Stability is an important indicator to quantify the device^[53] and previous work demonstrated that SC processed devices show improved thermal stability, which benefited from the formation of the robust polymer network during SC process.^[29,54,55] In order to get closer to the application scenario, we tested the photostability under maximum power point (MPP) conditions and found that SC-type devices showed advantages (Figure 5e and Figures S18–S22, Supporting Information). Since the storage stability in the nitrogen atmosphere of the two types of the encapsulated devices differs slightly (Figure S19, Supporting Information), it is argued that the influence of light

may be the main cause and we carried out photoaging experiments (Figures S20–S22, Supporting Information). It is found that the intrinsic stability of PM6 film and the pristine IT-4F are the poorest among all the pristine and blend films. For the blend films, the donor and acceptor of the PM6:IT-4F system is greatly affected simultaneously, while the donors in the PM6:PC₇₁BM and PM6:L8-BO systems experience more severe decay compared with acceptors. It is also found that the SC-type films show a subtle advantage in the photoaging process (Figure S22, Supporting Information). Based on the SIPS model, the amorphous and semicrystalline regions in polymer film are more susceptible to swelling, and a more delicate interpenetrating network is finally formed in SC processing. Therefore, we correlate the better photostability of SC-processed films with the swollen donor region and the more delicate D:A interpenetrating network. To further demonstrate the superiority of the SC processing method, we fabricated the 1 cm² devices (Figure 5f). The results show that the SC-type device exhibits higher J_{sc} and FF (Table S13, Supporting Information), leading to a higher PCE (16.50%) than that of a BC-type device (15.66%). In addition, the response ranges that achieve EQE gain (Figure 5g) are very similar to that in Figure 2g. This indicates that the SC processing has certain prospects for upscaled device fabrication.

3. Conclusion

We have demonstrated the versatility and efficacy of the SC method for fabricating BHJ-based OSCs with diverse D:A pairs, that is, PM6:PC₇₁BM, PM6:IT-4F and PM6:L8-BO. Improvement in device performance has been generally observed in all cases. Particularly, the SC method enables a record efficiency of 18.86% for the PM6:L8-BO solar cells (certified as 18.44%), and this represents the best-performing D:A binary OSC, demonstrating the effectiveness of sequential deposition for device optimization. Further, we propose the SIPS model to describe the film formation process during the sequential deposition, and this model explains some counterintuitive phase separation observations well. Based on the PM6:L8-BO system, we observe that the vertical phase segregation affects the device performance via affecting the charge transport and

recombination processes. These results are helpful in understanding the film morphology evolution and further developing high-performance OSCs.

Supporting Information

Supporting Information is available from the Wiley Online Library or from the author.

Acknowledgements

This work was supported by the National Natural Science Foundation of China (Nos. 21734008, 52173185, 5212780017, 61721005), National Key Research and Development Program of China (Nos. 2019YFA0705900), and Research Start-up Fund from Zhejiang University. RSoXS data were acquired at beamlines 7.3.3 and 11.0.1.2 at the Advanced Light Source, which is supported by the Director, Office of Science, Office of Basic Energy Sciences, of the U.S. Department of Energy under Contract No. DE-AC02-05CH11231. The authors thank Eric Schaible and Chenhui Zhu at Beamline 7.3.3, and Cheng Wang at beamline 11.0.1.2 for assistance with data acquisition. The authors are grateful for the technical support for Nano-X from Suzhou Institute of Nano-Tech and Nano-Bionics, Chinese Academy of Sciences.

Conflict of Interest

The authors declare no conflict of interest.

Data Availability Statement

The data that support the findings of this study are available from the corresponding author upon reasonable request.

Keywords

binary devices, bulk-heterojunctions, organic solar cells, phase-separation, sequential casting

Received: April 14, 2022
Revised: June 13, 2022
Published online: July 17, 2022

- [1] O. Inganäs, *Adv. Mater.* **2018**, *30*, 1800388.
- [2] J. Hou, O. Inganäs, R. H. Friend, F. Gao, *Nat. Mater.* **2018**, *17*, 119.
- [3] P. Cheng, G. Li, X. Zhan, Y. Yang, *Nat. Photonics* **2018**, *12*, 131.
- [4] Y. Li, C. He, L. Zuo, F. Zhao, L. Zhan, X. Li, R. Xia, H. L. Yip, C. Z. Li, X. Liu, H. Chen, *Adv. Energy Mater.* **2021**, *11*, 2003408.
- [5] S. Li, C.-Z. Li, M. Shi, H. Chen, *ACS Energy Lett.* **2020**, *5*, 1554.
- [6] Q. Shen, C. He, S. Li, L. Zuo, M. Shi, H. Chen, *Acc. Mater. Res.* **2022**, *3*, 644.
- [7] G. Yu, J. Gao, J. C. Hummelen, F. Wudl, A. J. Heeger, *Science* **1995**, *270*, 1789.
- [8] Y. Huang, E. J. Kramer, A. J. Heeger, G. C. Bazan, *Chem. Rev.* **2014**, *114*, 7006.
- [9] L. Zuo, S. B. Jo, Y. Li, Y. Meng, R. J. Stoddard, Y. Liu, F. Lin, X. Shi, F. Liu, H. W. Hillhouse, D. S. Ginger, H. Chen, A. K. Jen, *Nat. Nanotechnol.* **2022**, *17*, 53.
- [10] Y. Lin, J. Wang, Z. G. Zhang, H. Bai, Y. Li, D. Zhu, X. Zhan, *Adv. Mater.* **2015**, *27*, 1170.
- [11] S. Li, L. Zhan, F. Liu, J. Ren, M. Shi, C. Z. Li, T. P. Russell, H. Chen, *Adv. Mater.* **2018**, *30*, 1705208.
- [12] J. Yuan, T. Huang, P. Cheng, Y. Zou, H. Zhang, J. L. Yang, S. Y. Chang, Z. Zhang, W. Huang, R. Wang, D. Meng, F. Gao, Y. Yang, *Nat. Commun.* **2019**, *10*, 570.
- [13] J. Yuan, Y. Zhang, L. Zhou, G. Zhang, H.-L. Yip, T.-K. Lau, X. Lu, C. Zhu, H. Peng, P. A. Johnson, M. Leclerc, Y. Cao, J. Ulanski, Y. Li, Y. Zou, *Joule* **2019**, *3*, 1140.
- [14] C. He, Z. Chen, T. Wang, Z. Shen, Y. Li, J. Zhou, J. Yu, H. Fang, Y. Li, S. Li, X. Lu, W. Ma, F. Gao, Z. Xie, V. Coropceanu, H. Zhu, J.-L. Bredas, L. Zuo, H. Chen, *Nat. Commun.* **2022**, *13*, 2598.
- [15] S. Li, L. Zhan, Y. Jin, G. Zhou, T. K. Lau, R. Qin, M. Shi, C. Z. Li, H. Zhu, X. Lu, F. Zhang, H. Chen, *Adv. Mater.* **2020**, *32*, 2001160.
- [16] C. He, Y. Pan, Y. Ouyang, Q. Shen, Y. Gao, K. Yan, J. Fang, Y. Chen, C.-Q. Ma, J. Min, C. Zhang, L. Zuo, H. Chen, *Energy Environ. Sci.* **2022**, *15*, 2537.
- [17] L. Zhan, S. Li, X. Xia, Y. Li, X. Lu, L. Zuo, M. Shi, H. Chen, *Adv. Mater.* **2021**, *33*, 2007231.
- [18] C. He, Z. Bi, Z. Chen, J. Guo, X. Xia, X. Lu, J. Min, H. Zhu, W. Ma, L. Zuo, H. Chen, *Adv. Funct. Mater.* **2022**, *32*, 2112511.
- [19] L. Zhan, S. Li, T.-K. Lau, Y. Cui, X. Lu, M. Shi, C.-Z. Li, H. Li, J. Hou, H. Chen, *Energy Environ. Sci.* **2020**, *13*, 635.
- [20] S. Li, L. Zhan, C. Sun, H. Zhu, G. Zhou, W. Yang, M. Shi, C. Z. Li, J. Hou, Y. Li, H. Chen, *J. Am. Chem. Soc.* **2019**, *141*, 3073.
- [21] Y. Li, Y. Guo, Z. Chen, L. Zhan, C. He, Z. Bi, N. Yao, S. Li, G. Zhou, Y. Yi, Y. Yang, H. Zhu, W. Ma, F. Gao, F. Zhang, L. Zuo, H. Chen, *Energy Environ. Sci.* **2022**, *15*, 855.
- [22] C. He, Y. Li, Y. Liu, Y. Li, G. Zhou, S. Li, H. Zhu, X. Lu, F. Zhang, C.-Z. Li, H. Chen, *J. Mater. Chem. A* **2020**, *8*, 18154.
- [23] S. Li, L. Zhan, N. Yao, X. Xia, Z. Chen, W. Yang, C. He, L. Zuo, M. Shi, H. Zhu, X. Lu, F. Zhang, H. Chen, *Nat. Commun.* **2021**, *12*, 4627.
- [24] L. Zhan, S. Li, Y. Li, R. Sun, J. Min, Z. Bi, W. Ma, Z. Chen, G. Zhou, H. Zhu, M. Shi, L. Zuo, H. Chen, *Joule* **2022**, *6*, 662.
- [25] C. He, Y. Li, S. Li, Z. P. Yu, Y. Li, X. Lu, M. Shi, C. Z. Li, H. Chen, *ACS Appl. Mater. Interfaces* **2020**, *12*, 16700.
- [26] L. Zhu, M. Zhang, J. Xu, C. Li, J. Yan, G. Zhou, W. Zhong, T. Hao, J. Song, X. Xue, Z. Zhou, R. Zeng, H. Zhu, C. C. Chen, R. C. I. MacKenzie, Y. Zou, J. Nelson, Y. Zhang, Y. Sun, F. Liu, *Nat. Mater.* **2022**, *21*, 656.
- [27] Z. Zheng, J. Wang, P. Bi, J. Ren, Y. Wang, Y. Yang, X. Liu, S. Zhang, J. Hou, *Joule* **2022**, *6*, 171.
- [28] J. J. van Franeker, M. Turbiez, W. Li, M. M. Wienk, R. A. Janssen, *Nat. Commun.* **2015**, *6*, 6229.
- [29] J. C. Aguirre, S. A. Hawks, A. S. Ferreira, P. Yee, S. Subramaniyan, S. A. Jenekhe, S. H. Tolbert, B. J. Schwartz, *Adv. Energy Mater.* **2015**, *5*, 1402020.
- [30] D. H. Kim, J. Mei, A. L. Ayzner, K. Schmidt, G. Giri, A. L. Appleton, M. F. Toney, Z. Bao, *Energy Environ. Sci.* **2014**, *7*, 1103.
- [31] S. A. Hawks, J. C. Aguirre, L. T. Schelhas, R. J. Thompson, R. C. Huber, A. S. Ferreira, G. Zhang, A. A. Herzing, S. H. Tolbert, B. J. Schwartz, *J. Phys. Chem. C* **2014**, *118*, 17413.
- [32] X. Li, L. Cao, X. Yu, X. Du, H. Lin, G. Yang, Z. Chen, C. Zheng, S. Tao, *Sol. RRL* **2022**, *6*, 2200076.
- [33] K. Weng, L. Ye, L. Zhu, J. Xu, J. Zhou, X. Feng, G. Lu, S. Tan, F. Liu, Y. Sun, *Nat. Commun.* **2020**, *11*, 2855.
- [34] K. Jiang, J. Zhang, Z. Peng, F. Lin, S. Wu, Z. Li, Y. Chen, H. Yan, H. Ade, Z. Zhu, A. K. Jen, *Nat. Commun.* **2021**, *12*, 468.
- [35] Y. Zhang, K. Liu, J. Huang, X. Xia, J. Cao, G. Zhao, P. W. K. Fong, Y. Zhu, F. Yan, Y. Yang, X. Lu, G. Li, *Nat. Commun.* **2021**, *12*, 4815.
- [36] R. Sun, Q. Wu, J. Guo, T. Wang, Y. Wu, B. Qiu, Z. Luo, W. Yang, Z. Hu, J. Guo, M. Shi, C. Yang, F. Huang, Y. Li, J. Min, *Joule* **2020**, *4*, 407.

- [37] R. Sun, J. Guo, C. Sun, T. Wang, Z. Luo, Z. Zhang, X. Jiao, W. Tang, C. Yang, Y. Li, J. Min, *Energy Environ. Sci.* **2019**, *12*, 384.
- [38] M. Zhang, X. Guo, W. Ma, H. Ade, J. Hou, *Adv. Mater.* **2015**, *27*, 4655.
- [39] Y. Cui, H. Yao, L. Hong, T. Zhang, Y. Xu, K. Xian, B. Gao, J. Qin, J. Zhang, Z. Wei, J. Hou, *Adv. Mater.* **2019**, *31*, 1808356.
- [40] C. Li, J. Zhou, J. Song, J. Xu, H. Zhang, X. Zhang, J. Guo, L. Zhu, D. Wei, G. Han, J. Min, Y. Zhang, Z. Xie, Y. Yi, H. Yan, F. Gao, F. Liu, Y. Sun, *Nat. Energy* **2021**, *6*, 605.
- [41] S. Dai, M. Li, J. Xin, G. Lu, P. Xue, Y. Zhao, Y. Liu, M. Sun, L. Yu, Z. Tang, G. Lu, W. Ma, X. Zhan, *J. Mater. Chem. A* **2022**, *10*, 1948.
- [42] X. Li, R. Zhu, Z. He, X. Du, H. Lin, C. Zheng, G. Yang, Z. Chen, S. Tao, *ACS Appl. Mater. Interfaces* **2022**, *14*, 25842.
- [43] A. K. Kyaw, D. H. Wang, D. Wynands, J. Zhang, T. Q. Nguyen, G. C. Bazan, A. J. Heeger, *Nano Lett.* **2013**, *13*, 3796.
- [44] L. Zhang, B. Lin, B. Hu, X. Xu, W. Ma, *Adv. Mater.* **2018**, *30*, 1800343.
- [45] J. Zhao, Y. Li, G. Yang, K. Jiang, H. Lin, H. Ade, W. Ma, H. Yan, *Nat. Energy* **2016**, *1*, 15027.
- [46] J. Mai, Y. Xiao, G. Zhou, J. Wang, J. Zhu, N. Zhao, X. Zhan, X. Lu, *Adv. Mater.* **2018**, *30*, 1802888.
- [47] Q. Liu, Y. Jiang, K. Jin, J. Qin, J. Xu, W. Li, J. Xiong, J. Liu, Z. Xiao, K. Sun, S. Yang, X. Zhang, L. Ding, *Sci. Bull.* **2020**, *65*, 272.
- [48] Y. Wei, J. Yu, L. Qin, H. Chen, X. Wu, Z. Wei, X. Zhang, Z. Xiao, L. Ding, F. Gao, H. Huang, *Energy Environ. Sci.* **2021**, *14*, 2314.
- [49] L. Bu, S. Gao, W. Wang, L. Zhou, S. Feng, X. Chen, D. Yu, S. Li, G. Lu, *Adv. Electron. Mater.* **2016**, *2*, 1600359.
- [50] Z. Wang, Y. Hu, T. Xiao, Y. Zhu, X. Chen, L. Bu, Y. Zhang, Z. Wei, B. B. Xu, G. Lu, *Adv. Opt. Mater.* **2019**, *7*, 1900152.
- [51] T. Xiao, J. Wang, S. Yang, Y. Zhu, D. Li, Z. Wang, S. Feng, L. Bu, X. Zhan, G. Lu, *J. Mater. Chem. A* **2020**, *8*, 401.
- [52] I. Riedel, J. Parisi, V. Dyakonov, L. Lutsen, D. Vanderzande, J. C. Hummelen, *Adv. Funct. Mater.* **2004**, *14*, 38.
- [53] Q. Burlingame, M. Ball, Y.-L. Loo, *Nat. Energy* **2020**, *5*, 947.
- [54] H. Hwang, H. Lee, S. Shafian, W. Lee, J. Seok, K. Y. Ryu, D. Yeol Ryu, K. Kim, *Polymers* **2017**, *9*, 456.
- [55] S. Dong, K. Zhang, B. Xie, J. Xiao, H.-L. Yip, H. Yan, F. Huang, Y. Cao, *Adv. Energy Mater.* **2019**, *9*, 1802832.